European Journal of Mechanics / A Solids 115 (2026) 105820

Contents lists available at ScienceDirect

European Journal of Mechanics / A Solids

journal homepage: www.elsevier.com/locate/ejmsol

Full length article

Failure of shape-memory polymers: Experimentation and modeling

Mohit Goswami [a,*], Matteo Arricca [b], Lorenzo Bonetti [b], Stefano Pandini [c], Giulia Scalet [b], Konstantin Volokh [a]

[a] Faculty of Civil and Environmental Engineering, Technion - Israel Institute of Technology, Haifa, 3200003, Israel
[b] Department of Civil Engineering and Architecture, University of Pavia, via Ferrata 3, Pavia 27100, Italy
[c] Department of Mechanical and Industrial Engineering, University of Brescia, via Branze 38, Brescia 25133, Italy

ARTICLE INFO

Keywords:
Bulge test
Shape-memory polymers
Failure
Energy limiters

ABSTRACT

Driven by practical applications, studies on the thermo-mechanics of shape-memory polymers (SMPs) grew in quantity and quality. Most of these studies are focused on experiments and modeling of the SMP deformation including phase transition. Various theories with essentially different approaches are available and compete. The present work deals with the less explored issue related to the SMP failure. Results of conducted experimental studies of the onset of damage are reported for a polymer whose shape-memory behavior is based on a glass transition temperature. These results are obtained under uniaxial tension as well as via bulge – membrane inflation – tests under varying temperatures. The combination of these tests provides a better understanding of SMP behavior, compared to the popular, and easier to perform, purely uniaxial tension tests which might give an inaccurate view of material response. Experimental results are further used for calibrating hyperelastic models of glassy and rubbery phases of the SMP material. Two novel features of the theory include a simple switch between descriptions of glassy and rubbery phases and enforcement of energy limiters in the constitutive equations to account for material failure. A general theoretical setting is also provided for modeling cracks, yet they are not simulated in the present work.

1. Introduction

Shape-memory polymers (SMPs) are smart soft materials characterized by the capability of switching between a previously imposed temporary shape to their "original" permanent shape, under the application of an external stimulus, *e.g.*, heat, light, magnetic field. Such an outcome is termed one-way shape-memory effect (SME). Its combination with some advantageous features of SMPs as low cost and weight, good processability, possible biocompatibility, high shape deformability and recoverability, makes SMPs suitable materials for several applications such as biomedical and pharmaceutical (Xia et al., 2021), aerospace (Meng and Hu, 2009; Scalet, 2020), and 4D fabrication (Jiang et al., 2022; Bonetti et al., 2024).

The thermally-driven one-way SME is likely the most studied effect. It results from a combination of the polymer macromolecular architecture with the application of a specific thermo-mechanical history, known as shape-memory cycle, above and below the so-called transition temperature. The latter, for typical SMPs, is the glassy temperature, named T_g hereafter, and two distinct states characterize the polymer architecture above and below T_g, often referred to as the rubbery and the glassy, or frozen, phase, respectively. The one-way shape-memory cycle involves the heating of the material above T_g under an applied load, followed by cooling below T_g to achieve the programmed temporary shape prior to load removal. The temporary stored shape at low temperatures evolves by reheating the material, which reverts to its permanent shape above the transition temperature.

Several models have been proposed over the years to describe and characterize the shape-memory behavior of such smart materials. Two well-defined main approaches can be identified. The early works of Tobushi et al. (1996, 1997, 1998) have paved the way to constitutive *rheological* models of SMPs, starting from modification on the standard theory of linear viscoelasticity. *Phase transition* models have been developed from the pioneering work of Liu et al. (2006), which are based on the introduction of *phase* variables, assumption of equality of stresses (strains) between the two phases of the material, and the rule of mixtures applied to characterize the strain (stress) response. Lastly, a combination of the two aforementioned approaches has also been adopted since the framework proposed by Qi et al. (2008). A detailed review and discussion of these approaches is out of the scope of this work; the reader is referred to comprehensive reviews such as Hu et al. (2012), Nguyen (2013), Yan and Li (2022) and Zhao et al. (2023).

While many groups have been working intensely on the constitutive modeling of SMPs and their composites, very few studies of failure and

* Corresponding author.
E-mail addresses: mohit@technion.ac.il (M. Goswami), giulia.scalet@unipv.it (G. Scalet), cvolokh@technion.ac.il (K. Volokh).

https://doi.org/10.1016/j.euromechsol.2025.105820
Received 29 May 2025; Received in revised form 8 July 2025; Accepted 28 July 2025
Available online 5 August 2025

fracture are available, e.g. Foyouzat et al. (2020, 2021) and Konale and Srivastava (2025). These studies are desirable for several application fields of SMPs where durability and strength are highly important, such as soft robots and actuators. In the latter applications SMPs experience multiaxial states of stress and may be prone to several damaging modes.

Following Volokh (2025), we distinguish between material failure and fracture and we define the former as the onset of damage via material instability and the latter as the damage localization and propagation via cracks. We note that analysis of failure without fracture might be the most important constraint for the design of SMP-based structures.

The present work aims to study the failure of thermo-responsive one-way SMPs through a combined experimental and theoretical investigation.

In particular, we first carry out tests with a commercial thermoplastic polyurethane exhibiting the one-way SME based on the glass transition, to characterize its failure behavior and its shape-memory performances under both uniaxial and equibiaxial state of stress. Stiffness of soft materials is routinely evaluated via uniaxial/equibiaxial tests, where uniform stress–strain states facilitate straightforward calibration. By contrast, strength calibration presents greater complexity: equibiaxial tests are highly sensitive to boundary conditions, often yielding misleading failure predictions. This limitation underscores the necessity of bulge tests, which localize failure at the membrane apex under pure equi-biaxial stress—entirely insensitive to boundary effects.

In the bulge test, the stress–strain state is not uniform and the maximum equibiaxial stresses and strains develop on the top of the inflated membrane, where the damage also starts (Goswami et al., 2024). Localization of damage on the top of the membrane provides robust testing processes unaffected by the boundary conditions. Unluckily, the payment for the test robustness is high – the theoretical interpretation of the experimental results is not trivial.

In addition to experiments, we develop a theoretical model to predict deformation and failure of SMPs. The free energy is formulated in such a way to take into account the different amorphous and glassy phases within the T_g - based SMP. The iterative curve fitting procedure developed in Lev et al. (2019) is further implemented to calibrate material parameters based on the combination of the results of uniaxial tension and bulge tests. Lastly, calibrated material models are used to evaluate the critical hydrostatic tension indicating the onset of cavitation under the varying temperatures.

The rest of the paper is organized as follows. Material preparation and its experimental characterization are introduced in Section 2. Section 3 deals with the definition of the constitutive theory and the characterization of the stress response of the material, whereas Section 4 presents and discusses the numerical results and model validation. Conclusions in Section 5 complete the manuscript.

2. Experiments

This section presents the materials and methods adopted for the preparation and characterization of the experimental samples.

2.1. Materials

Films were fabricated from a commercial aromatic shape-memory polyether urethane (DiAPLEX MM 3520, SMP Technologies Inc., Tokyo, Japan), hereafter referred to as TPU. According to the supplier's technical datasheet, TPU pellet was subjected to a dehumidification step in an oven (80 °C, 4 h).

2.2. Film preparation

TPU pellet (25 g) was placed between two polytetrafluoroethylene (PTFE) sheets and inserted in a hot press (International crystal laboratories, Garfield, USA) at 180 °C, 1000 psi, for 5 min. After cooling to room temperature, TPU films were easily detached from the PTFE sheets. By means of a cutter, 100 × 100 × 1 mm ($l \times w \times h$) specimens were obtained for further testing.

2.3. Thermal characterization

The thermal properties of the specimens were investigated by Differential Scanning Calorimetry (DSC 250, TA Instruments). Specimens were first conditioned at 75 °C, then cooled to −5 °C (2 °C/min ramp). After an isothermal step (−5 °C, 5 min), the specimens were heated to 75 °C (2 °C/min). The glass transition temperature, T_g, was determined from the heating curve by means of half-height analysis.

The coefficient of thermal expansion, γ, was measured using a Dynamic Mechanical Analyzer (DMA Q850, TA Instruments) in the tensile mode. After an initial preconditioning step (10 min, T = –10 °C, pre-load = 0.001 N), the specimens were heated (2 °C/min) up to 90 °C in iso-stress conditions (0.001 N). Evaluation of γ was performed as the slope of the strain–temperature curve (Volk et al., 2010) in two ranges: 10–20 °C (*i.e.*, $T < T_g$) and 35–45 °C (*i.e.*, $T > T_g$). From now on, the coefficient is denoted as γ_g and γ_r for the glassy (*i.e.*, $T < T_g$) and rubbery (*i.e.*, $T > T_g$) phase, respectively.

2.4. Uniaxial mechanical characterization

Uniaxial tensile tests were carried out by electro-mechanical dynamometer (Instron 3366) on rectangular TPU strips, with an overall length greater than 50 mm (gauge length, l_0: 30 mm) and width equal to about 5 mm (clamp width: 50 mm). The tests were performed up to final rupture with a crosshead speed equal to 15 mm/min (strain rate: 0.5 min^{-1}). Nominal (engineering) stress and strain along the direction of force application were evaluated as $P_u = f/A_0$ and $\epsilon_u = \Delta l/l_0$ respectively, where f is the measured force, Δl is the crosshead displacement, A_0 is the initial specimen cross-section, and l_0 is the gauge length.

Data obtained from uniaxial tensile tests were plotted in stress–strain curves. For each curve, the considered mechanical parameters were the Young's modulus, E (calculated as the slope of the curve in the first most linear part of the curve (T_{amb}, 0.05%–0.25% strain range, $R^2 > 0.97$; T_{80} 0.1%–1% strain range, $R^2 > 0.6$), the stress at break, $\sigma_{\max}$, and the strain at break, $\epsilon_{\max}$.

2.5. Uniaxial shape-memory characterization

One-way shape-memory characterization of the specimens was carried out using a Dynamic Mechanical Analyzer (DMA Q850, TA Instruments) in the uniaxial tensile mode. After an initial preconditioning step (10 min, T = 80 °C, pre-load = 0.001 N), a strain ramp (30%/min) was applied at 80 °C up to ϵ_{appl} (nominal). Then, a cooling step (2 °C/min) down to 27 °C (*i.e.*, $T < T_g$) was carried out keeping the strain fixed (ϵ_{appl} = 10% or 20% nominal). The specimen was then unloaded (f = 0.001 N) and heated (2 °C/min) up to 80 °C under quasi-stress-free conditions.

The ability of the material to be set in a temporary shape was quantified in terms of strain fixity ratio (Bonetti et al., 2024): $R_f = 100(\epsilon_{unload}/\epsilon_{appl})$, where ϵ_{appl} represents the nominal strain applied before unloading and ϵ_{unload} the strain after load removal.

The ability of the material to recover its permanent shape after the quasi-stress-free heating ramp was quantified in terms of strain recovery ratio: $R_r = 100(\epsilon_{appl} - \epsilon_{rec})/\epsilon_{appl}$, where ϵ_{rec} represents the residual strain measured after the heating ramp.

2.6. Bulge tests and equibiaxial shape-memory characterization

The bulge test procedure is used to study equibiaxial state of stress. The latter investigation is performed using an in-house developed bulge test device. The schematic design of device is shown in Fig. 1. Three thermocouples are placed inside a thermal chamber to ensure uniform temperature. The pressure from compressor is regulated using a pressure flow controller and supplied to the device. The specimens of 1 mm thickness are clamped between bottom and top flanges. The

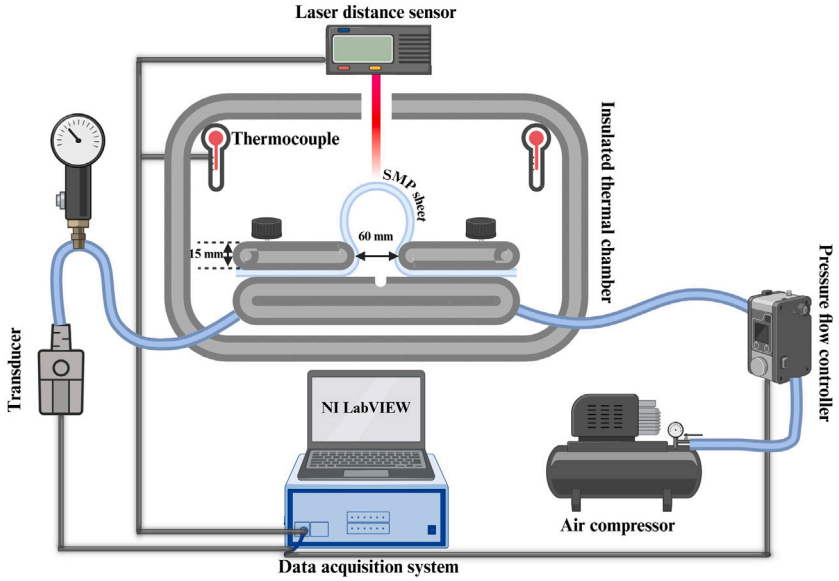

Fig. 1. Schematic representation of in-house developed bulge test device.

thickness of upper flange is 15 mm, and it has a hole of 60 mm diameter to allow inflation of the specimen. The pressure inside inflated specimen is monitored using a pressure transducer (range: 0–10 bar, 0.5% accuracy). During this process the vertical displacement at the center of specimen is acquired using a laser distance sensor. The data from all these monitoring devices are transmitted to a data acquisition system and further visualized using an NI LabVIEW program.

Bulge tests and equibiaxial shape-memory tests were carried out on the SMP films obtained. For bulge tests, the films were inflated up to failure in glassy (300 K) and rubbery (353 K) phases at a low pressure rate of 0.02 bar/s to avoid viscoelastic effects. Equibiaxial shape-memory tests were performed in four steps. First step involved inflation of specimen in rubbery phase to attain temporary shape, which was done at a pressure rate of 0.02 bar/s up to pressures of 0.45 bar, 0.6 bar, and 0.75 bar and the height of inflated specimen (δ_{appl}) was recorded. In second step, the specimens were cooled to 300 K while maintaining their respective pressures achieved in first step. Third step involved removing pressure applied and taking out specimen with temporary shape which provides the height of unloaded specimen (δ_{unload}). Lastly, they were reheated again to gain the original shape. For detailed elaboration please refer to Fig. 2. The shape fixity is calculated as: $R_f = 100(\delta_{unload}/\delta_{appl})$ and recovery ratio as: $R_r = 100(\delta_{appl} - \delta_{rec})/(\delta_{appl} - \delta_0)$, where δ_{rec} and δ_0 are vertical displacements obtained during reheating of specimen (step 4) and initial stage (prior to step 1), respectively. The relationships mentioned in Section 2.5 are further used to calculate R_f and R_r for equibiaxial results.

3. Theory

SMPs based on T_g enjoy two possible phases depending on the temperature: glassy ($T < T_g$) and rubbery ($T > T_g$). Strictly speaking, none of them is an ideally pure phase and, rather, a mixture of the phases with one of them dominant. Also, many SMPs exhibit some rate-dependence in mechanical response due to the internal friction. Above all, Mulins effect can be observed in the rubbery phase. All such subtleties are ignored in this work. We present the very basic theory on which the mentioned features can be superimposed if necessary.

3.1. General setting

An important feature of the kinematic description of the SMP mechanical response is the possibility of the so-called "frozen" deformation, which appears as a result of the phase transition in the loaded state (Boatti et al., 2016). We note that the frozen deformation is geometrically compatible and, thus, its gradient tensor $\mathbf{F}_f$ is defined globally and uniquely in contrast to the multiplicative decompositions of the deformation gradients in various theories of inelasticity. In the latter cases, the co-factors of the multiplicative decompositions are not unique and defined locally, which makes their physical interpretation difficult.

We set the specific (per unit mass) Helmholtz free energy as follows

$$w = \mathcal{H}(T - T_g)w_r(\mathbf{F}, T) + \{1 - \mathcal{H}(T - T_g)\}w_g(\mathbf{F}\mathbf{F}_f^{-1}, T), \tag{1}$$

and

$$\mathbf{F}_f = \text{constant} = \mathcal{H}(T(t-\delta) - T_g)\{1 - \mathcal{H}(T(t) - T_g)\}\mathbf{F}(t-\delta), \tag{2}$$

where $\mathcal{H}(x)$ is the Heaviside step function: $\mathcal{H}(x) = 0$ if x is negative and $\mathcal{H}(x) = 1$ otherwise; T is the absolute temperature; w_r and w_g are the specific free energies for rubbery and glassy states accordingly; $\mathbf{F}$ is the deformation gradient; $\mathbf{F}_f$ is the "frozen" deformation tensor, which is history-dependent; t is not necessary a physical time – it can be a loading parameter, for example; and δ is a small real number.

In view of the numerical implementation of the theory it is more convenient to set the free energy directly in the time-discretized form via successive time steps as t_{n-1} and t_n, where n defines the current time. We designate variables at the time points as follows: $T_k \equiv T(t_k)$; $w_k \equiv w(t_k)$; and $\mathbf{F}_k \equiv \mathbf{F}(t_k)$. Then, we can rewrite (1) and (2) in the form

$$w_n = \mathcal{H}(T_n - T_g)w_r(\mathbf{F}_n, T_n) + \{1 - \mathcal{H}(T_n - T_g)\}w_g(\mathbf{F}_n\mathbf{F}_f^{-1}, T_n), \tag{3}$$

and

$$\mathbf{F}_f = \text{constant} = \mathcal{H}(T_{n-1} - T_g)\{1 - \mathcal{H}(T_n - T_g)\}\mathbf{F}_{n-1}. \tag{4}$$

Remark 1. We emphasize that the tensor of frozen deformation is constant except for the time point of transition from the rubbery to glassy state: $\mathcal{H}(T(t-\delta) - T_g)\{1 - \mathcal{H}(T(t) - T_g)\} = 1$ or $\mathcal{H}(T_{n-1} - T_g)\{1 - \mathcal{H}(T_n - T_g)\} = 1$, where it changes its value to: $\mathbf{F}_f = \mathbf{F}(t-\delta)$ or $\mathbf{F}_f = \mathbf{F}_{n-1}$, otherwise $\mathbf{F}_f = \mathbf{1}$.

Following the standard path, we consider the dissipation inequality in the following form

$$D_{\text{int}} = \mathbf{P} : \dot{\mathbf{F}} - \varrho\dot{w} - \varrho\eta\dot{T} \geq 0, \tag{5}$$

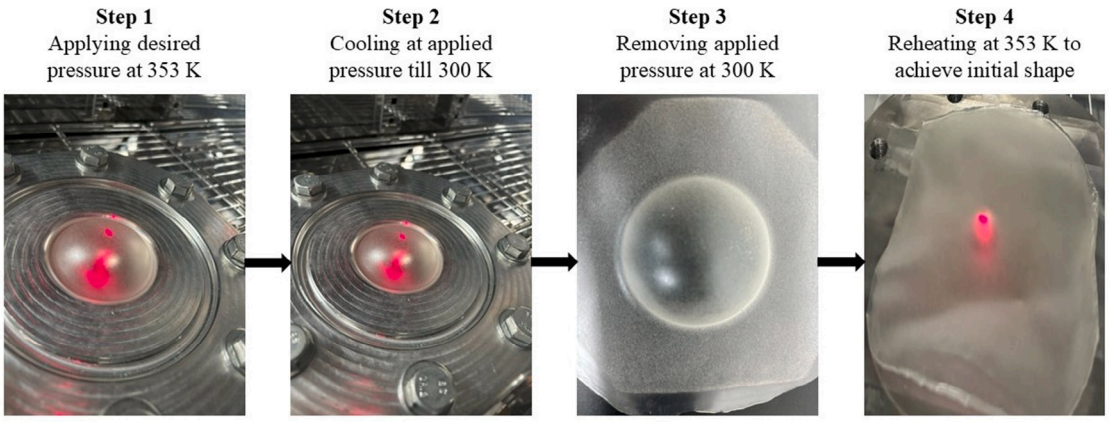

Fig. 2. Experimental protocol for shape-memory cyclic bulge tests.

where $\mathbf{P}$ is the first Piola–Kirchhoff; ϱ is the Lagrangian (referential) mass density; and η is the entropy per unit mass or specific entropy. With account of $\dot{w} = (\partial w/\partial \mathbf{F}) : \dot{\mathbf{F}} + (\partial w/\partial T)\dot{T}$ and after some manipulations, we can rewrite (5) in the form

$$D_{\text{int}} = (\mathbf{P} - \varrho \frac{\partial w}{\partial \mathbf{F}}) : \dot{\mathbf{F}} - \varrho \dot{T}(\eta + \frac{\partial w}{\partial T}) \geq 0, \tag{6}$$

and advised by Coleman and Noll, we set constitutive equations in the form

$$\mathbf{P} = \varrho \frac{\partial w}{\partial \mathbf{F}}, \qquad \eta = -\frac{\partial w}{\partial T}. \tag{7}$$

Introducing the initial mass density $\varrho_0 = \varrho(t = 0)$, we can rewrite the constitutive equations as

$$\mathbf{P} = \frac{\varrho}{\varrho_0} \frac{\partial W}{\partial \mathbf{F}}, \qquad \eta \varrho_0 = -\frac{\partial W}{\partial T}, \tag{8}$$

where $W = \varrho_0 w$ is the Helmholtz free energy per unit initial volume.

Importantly, the referential mass density, ϱ, is not constant and it is a variable because we account for the fracture process during which molecular bonds break in a small area. Such breakage is not confined to one surface — it is diffused. The diffused bond breakage leads, in its turn, to the local loss of material and the mass balance reads

$$\text{Div}\mathbf{s} + \xi = 0, \tag{9}$$

where $\mathbf{s}$ and ξ are the Lagrangian mass flux and source (sink) respectively.

The corresponding natural boundary conditions express this same mass balance law on the boundary

$$\mathbf{s} \cdot \mathbf{n} = 0, \tag{10}$$

in which $\mathbf{n}$ is a unit outward normal to the initial configuration.

Remark 2. We note that mass density also depends on time and, generally, the rate of mass density is nonzero. However, the change of mass due to the bond rupture is so fast as compared to the deformation and fracture processes that we can ignore it and set $\dot{\varrho} \approx 0$ (Volokh, 2025).

We choose the constitutive law for the mass flux and sink in the form

$$\mathbf{s} = \kappa \text{Grad}\varrho, \tag{11}$$

and

$$\xi = \beta \varrho_0 - \beta \varrho / \mathcal{K}, \tag{12}$$

where, now,

$$\mathcal{K} = \exp[-\mathcal{H}(T - T_{\text{g}}) W_{\text{r}}^m \Phi_{\text{r}}^{-m} - \{1 - \mathcal{H}(T - T_{\text{g}})\} W_{\text{g}}^p \Phi_{\text{g}}^{-p}], \tag{13}$$

in which $W_{\text{r}} = \varrho_0 w_{\text{r}}$ and $W_{\text{g}} = \varrho_0 w_{\text{g}}$ are free energies per initial volume for the rubbery and glassy states accordingly; and κ, β, m, p are material parameters. Φ_{r}, and Φ_{g} are energy limiters for rubbery and glassy phase, respectively.

It is possible to induce irreversibility of fracture in the analytical formulation above. In computations, however, it is easy to directly account for the irreversibility: $\mathcal{K}(t_0) \equiv \mathcal{K}_0 = 1$, and $\mathcal{K}(t_n) \equiv \mathcal{K}_n = \min\{\exp[-W^m \Phi^{-m}], \mathcal{K}_{n-1}\}$.

Substitution of (11), (12), and (13) in (9) yields

$$l^2 \text{DivGrad}\varrho = \varrho/\mathcal{K} - \varrho_0, \tag{14}$$

where $l = \sqrt{\kappa/\beta}$ is the characteristic length, which means that there is no need to define parameters κ and β separately.

Remark 3. We assume that the temperature changes are slow enough to ignore the heat flow and coupling with the energy balance equation. In other words, our analysis is purely thermoelastic.

The calibration of the characteristic length l is of central importance for modeling crack propagation. The estimate of the characteristic length for rubber is $l \sim 0.2$ mm (Volokh, 2011).

We note that the mass balance equation, in which the small characteristic length parameter is a co-factor of the highest spatial derivatives, provides solutions of the boundary-layer type. This solution gives the thin area of damage localization – crack.

The mass balance equation coupled with the momenta balance completes the initial boundary value problem describing fracture — damage localization and propagation. However, in many practical problems, e.g. design of structures, it is enough to consider only the nucleation or onset of damage. The latter initial stage of fracture can be called failure (Volokh, 2025). In the case of material failure mass flux is zero, $\mathbf{s} = \mathbf{0}$ and, consequently, $\xi = 0$ from (9). Setting zero on the left hand side of (12), we find the relative mass density : $\varrho/\varrho_0 = \mathcal{K}$. Substituting the relative mass density in the constitutive law for stresses, we get

$$\mathbf{P} = \mathcal{K} \frac{\partial W}{\partial \mathbf{F}}. \tag{15}$$

This equation describes hyperelasticity with the energy limiters (Volokh, 2025). It provides the upper bound for the strain energy – the energy that material can store and dissipate. Such bound automatically limits the maximal achievable stress – strength. Thus the very concept of strength is not separated from the stress analysis anymore and it is built-in in the constitutive description. We emphasize that the idea that the stored energy must be bounded has microscopic roots — the energy of molecular bonds is bounded and, consequently, the bulk energy must be bounded either. This is the fundamental physical observation, which does not require additional toy models of molecules in the form of joined springs and the like.

3.2. Specialization

We further specialize the free energies in terms of the generalized thermoelastic three-term Ogden models (Ogden, 1972, 1997; Lev et al., 2019) for isotropic material as

$$W_{\rm r} = \frac{T}{T_0}\sum_{i=1}^{3}\frac{\mu_{{\rm r}i}}{\alpha_{{\rm r}i}}(\lambda_1^{\alpha_{{\rm r}i}}+\lambda_2^{\alpha_{{\rm r}i}}+\lambda_3^{\alpha_{{\rm r}i}}-3)+c_0T_0\ln\left[\frac{T}{T_0}\right], \qquad \mu_{{\rm r}i}\alpha_{{\rm r}i}>0, \quad (16)$$

and

$$W_{\rm g} = \frac{T}{T_0}\sum_{i=1}^{3}\frac{\mu_{{\rm g}i}}{\alpha_{{\rm g}i}}(\lambda_1^{\alpha_{{\rm g}i}}+\lambda_2^{\alpha_{{\rm g}i}}+\lambda_3^{\alpha_{{\rm g}i}}-3)+c_0T_0\ln\left[\frac{T}{T_0}\right], \qquad \mu_{{\rm g}i}\alpha_{{\rm g}i}>0, \quad (17)$$

where $T_0 = 298$ K is the temperature at $t = 0$ and $\mu_{{\rm r}j}$, $\mu_{{\rm g}j}$, $\alpha_{{\rm r}j}$, $\alpha_{{\rm g}j}$, c_0 are material constants.

We assume that material is thermo-elastically incompressible, which means that all volume changes are due to temperature variations only,

$$J = \det\mathbf{F} = \exp\left[3\gamma\left(T-T_0\right)\right], \qquad \gamma = \mathcal{H}(T-T_{\rm g})\gamma_{\rm r}+\{1-\mathcal{H}(T-T_{\rm g})\}\gamma_{\rm g}, \quad (18)$$

where $\gamma_{\rm r}$ and $\gamma_{\rm g}$ are coefficients of thermal expansion for rubber and glassy phase, respectively. With the latter restriction, we can write the first Piola–Kirchhoff for rubbery and glassy phases as

$$\mathbf{P} = \mathcal{K}\frac{\partial W}{\partial\mathbf{F}} - \Pi J\mathbf{F}^{-\rm T}, \quad (19)$$

where Π is the Lagrange multiplier. Furthermore, the first Piola–Kirchhoff combining both the phases can be written as

$$\mathbf{P} = \mathcal{H}(T-T_{\rm g})\mathbf{P}_{\rm r}+\{1-\mathcal{H}(T-T_{\rm g})\}\mathbf{P}_{\rm g}, \quad (20)$$

with

$$\mathbf{P}_{\rm r} = \mathcal{K}\frac{\partial W_{\rm r}}{\partial\mathbf{F}} - \Pi_{\rm r}J\mathbf{F}^{-\rm T}, \quad (21)$$

and

$$\mathbf{P}_{\rm g} = \mathcal{K}\frac{\partial W_{\rm g}}{\partial\mathbf{F}} - \Pi_{\rm g}J(\mathbf{F}\mathbf{F}_{\rm f}^{-1})^{-\rm T}. \quad (22)$$

3.2.1. Uniaxial tension

Considering homogeneous deformations, the deformation gradient in terms of Cartesian basis vectors $\mathbf{e}_1, \mathbf{e}_2, \mathbf{e}_3$ and corresponding stretches $\lambda_1, \lambda_2, \lambda_3$ can be expressed as follows

$$\mathbf{F} = \lambda_1\mathbf{e}_1\otimes\mathbf{e}_1+\lambda_2\mathbf{e}_2\otimes\mathbf{e}_2+\lambda_3\mathbf{e}_3\otimes\mathbf{e}_3, \quad (23)$$

and, for uniaxial tension, we get

$$\lambda_1 = \lambda, \qquad \lambda_2 = \lambda_3 = \sqrt{\frac{J}{\lambda}}. \quad (24)$$

Then, the nonzero components of the Piola–Kirchhoff stresses for rubbery phase can be written as

$$P_{\rm r1} = \mathcal{K}\frac{\partial W_{\rm r}}{\partial\lambda_1} - \frac{\Pi_{\rm r}J}{\lambda_1}, \qquad P_{\rm r2} = \mathcal{K}\frac{\partial W_{\rm r}}{\partial\lambda_2} - \frac{\Pi_{\rm r}J}{\lambda_2}, \qquad P_{\rm r3} = \mathcal{K}\frac{\partial W_{\rm r}}{\partial\lambda_3} - \frac{\Pi_{\rm r}J}{\lambda_3}. \quad (25)$$

Since there are no lateral stresses in uniaxial tension, we set $P_{\rm r2} = P_{\rm r2} = 0$, and find the Lagrange multiplier

$$\Pi_{\rm r} = \frac{\mathcal{K}}{J}\frac{T}{T_0}\sum_{i=1}^{3}\mu_{{\rm r}i}\left(\sqrt{\frac{J}{\lambda}}\right)^{\alpha_{{\rm r}i}}. \quad (26)$$

Then, the axial Piola–Kirchhoff stress is

$$P_{\rm r} = \frac{\exp(-W_{\rm r}^m\Phi_{\rm r}^{-m})}{\lambda}\frac{T}{T_0}\sum_{i=1}^{3}\mu_{{\rm r}i}\left\{\lambda^{\alpha_{{\rm r}i}}-\left(\sqrt{\frac{J}{\lambda}}\right)^{\alpha_{{\rm r}i}}\right\}, \quad (27)$$

and the Cauchy stress is

$$\sigma_{\rm r} = \frac{\exp(-W_{\rm r}^m\Phi_{\rm r}^{-m})}{J}\frac{T}{T_0}\sum_{i=1}^{3}\mu_{{\rm r}i}\left\{\lambda^{\alpha_{{\rm r}i}}-\left(\sqrt{\frac{J}{\lambda}}\right)^{\alpha_{{\rm r}i}}\right\}. \quad (28)$$

Similarly, we can calculate stresses for the glassy phase

$$P_{\rm g} = \exp(-W_{\rm g}^p\Phi_{\rm g}^{-p})\frac{\lambda_{\rm f}T}{\lambda T_0}\sum_{i=1}^{3}\mu_{{\rm g}i}\left\{\left(\frac{\lambda}{\lambda_{\rm f}}\right)^{\alpha_{{\rm g}i}}-\left(\sqrt{\frac{J\lambda_{\rm f}}{\lambda}}\right)^{\alpha_{{\rm g}i}}\right\}, \quad (29)$$

and

$$\sigma_{\rm g} = \frac{\exp(-W_{\rm g}^p\Phi_{\rm g}^{-p})}{J}\frac{T}{T_0}\sum_{i=1}^{3}\mu_{{\rm g}i}\left\{\left(\frac{\lambda}{\lambda_{\rm f}}\right)^{\alpha_{{\rm g}i}}-\left(\sqrt{\frac{J\lambda_{\rm f}}{\lambda}}\right)^{\alpha_{{\rm g}i}}\right\}, \quad (30)$$

where $\lambda_{\rm f}$ is a constant principal stretch corresponding to the frozen deformation.

3.2.2. Equibiaxial tension

For the equibiaxial tension, we have the following principal stretches

$$\lambda_1 = \lambda_2 = \lambda, \qquad \lambda_3 = \frac{J}{\lambda^2}, \quad (31)$$

and set $P_{\rm r3} = 0$ in Eq. (25), and calculate the Lagrange multiplier

$$\Pi_{\rm r} = \frac{\mathcal{K}}{J}\frac{T}{T_0}\sum_{i=1}^{3}\mu_{{\rm r}i}\left(\frac{J}{\lambda^2}\right)^{\alpha_{{\rm r}i}}. \quad (32)$$

Then, the stresses for equibiaxial tension take form

$$P_{\rm r} = \frac{\exp(-W_{\rm r}^m\Phi_{\rm r}^{-m})}{\lambda}\frac{T}{T_0}\sum_{i=1}^{3}\mu_{{\rm r}i}\left\{\lambda^{\alpha_{{\rm r}i}}-\left(\frac{J}{\lambda^2}\right)^{\alpha_{{\rm r}i}}\right\}, \quad (33)$$

$$\sigma_{\rm r} = \frac{\exp(-W_{\rm r}^m\Phi_{\rm r}^{-m})}{J}\frac{T}{T_0}\sum_{i=1}^{3}\mu_{{\rm r}i}\left\{\lambda^{\alpha_{{\rm r}i}}-\left(\frac{J}{\lambda^2}\right)^{\alpha_{{\rm r}i}}\right\}, \quad (34)$$

$$P_{\rm g} = \exp(-W_{\rm g}^p\Phi_{\rm g}^{-p})\frac{\lambda_{\rm f}T}{\lambda T_0}\sum_{i=1}^{3}\mu_{{\rm g}i}\left\{\left(\frac{\lambda}{\lambda_{\rm f}}\right)^{\alpha_{{\rm g}i}}-\left(\frac{\sqrt{J}\lambda_{\rm f}}{\lambda}\right)^{2\alpha_{{\rm g}i}}\right\}, \quad (35)$$

and

$$\sigma_{\rm g} = \frac{\exp(-W_{\rm g}^p\Phi_{\rm g}^{-p})}{J}\frac{T}{T_0}\sum_{i=1}^{3}\mu_{{\rm g}i}\left\{\left(\frac{\lambda}{\lambda_{\rm f}}\right)^{\alpha_{{\rm g}i}}-\left(\frac{\sqrt{J}\lambda_{\rm f}}{\lambda}\right)^{2\alpha_{{\rm g}i}}\right\}. \quad (36)$$

4. Results and discussions

This section discusses the experimental results obtained by performing uniaxial and bulge tests at various temperatures, as described in Section 2. The calibration of material parameters using the developed constitutive models is also performed. The experimental results are compared with numerical simulations for failure and shape-memory cycle tests.

4.1. Thermal properties

The glass transition temperature, $T_{\rm g}$, of the materials resulted equal to 31.45 °C based on DSC analysis. The coefficient of thermal expansion, γ, measured using a DMA, resulted equal to 7.47×10^{-5} K^{-1} in the range 10-20 °C (*i.e.*, $T < T_{\rm g}$) and to 1.34×10^{-4} K^{-1} in the range 35–45 °C (*i.e.*, $T > T_{\rm g}$).

4.2. The bulge tests

The results obtained from bulge tests performed in rubbery and glassy phases are shown in Fig. 3. The failure occurs at the very top of the inflated membrane where the state of stress is purely equibiaxial. The pressures at failure were 1.2 bar and 5.4 bar for rubbery and glassy states, respectively. However, the height of the membrane at the failure were recorded to be 35 mm and 26 mm, for rubbery and glassy states, respectively. Interpretation of these results is not trivial because of non-uniform distribution of strains throughout the inflated membrane. We use successive finite element simulations of the membrane inflation (Balakhovsky and Volokh, 2012) to fit theory

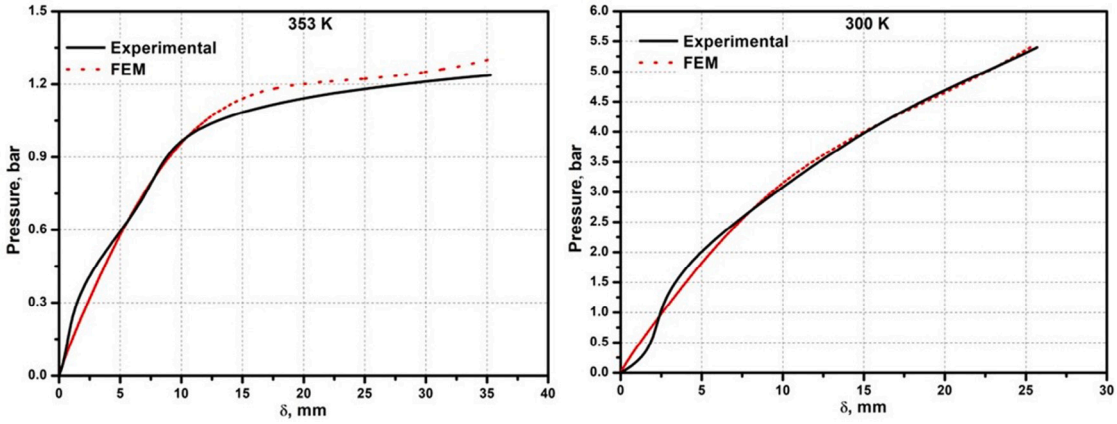

Fig. 3. Representative pressure versus height plots in rubbery (353 K) and glassy (300 K) state until failure.

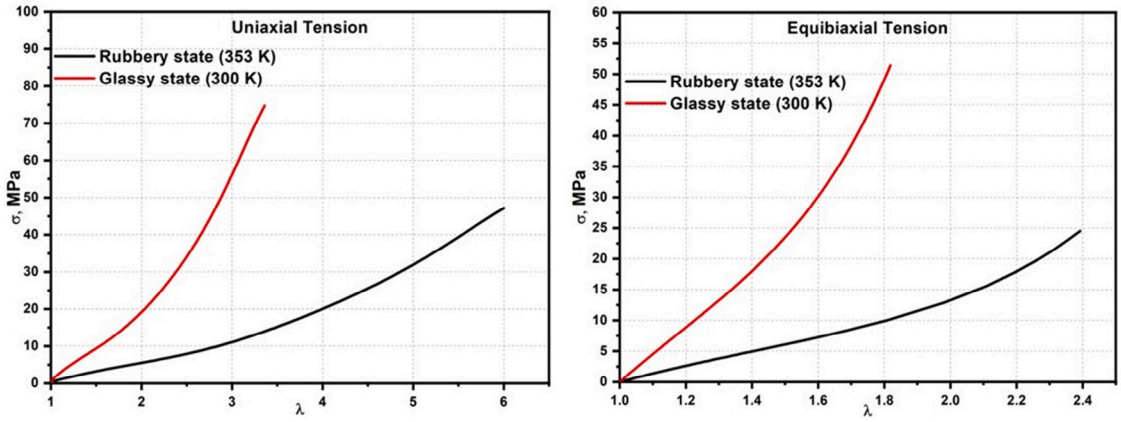

Fig. 4. Representative Cauchy stress versus stretch plots for uniaxial and equibiaxial tension in different states until failure.

– constitutive law – to the test results. Material parameters converge to the best correlation between experiment and theory. Comparisons between pressure versus height results obtained using experiments and simulations are shown in Fig. 3.

4.3. Uniaxial and equibiaxial tension

The experimental results obtained for uniaxial and equibiaxial tension, that is extracted from uniaxial experiments and the membrane inflation tests, are shown in Fig. 4 in terms of Cauchy stress and stretch. It can be seen that the stiffness of a material is higher in glassy phase when compared with the rubbery phase. The latter observations can be attributed to the reduction of chain mobility below T_g (as stated below) (the effect of density becomes particularly relevant as T increases for T > T_g) and their density in the glassy phase, which contributes significantly to increased stiffness.

The Cauchy stress at failure is found to be 66% and 80% more in glassy phase when compared with rubbery phase, for uniaxial and equibiaxial tension, respectively. However, the stretch at failure is 78% and 33% more in rubbery phase when compared with glassy phase, for uniaxial and equibiaxial tension, respectively. The latter observations can be attributed to the high rigidity of molecular chains in glassy phase, which restricts molecular mobility, whereas, the increased thermal energy in rubbery phase enhances mobility of polymeric chains (Lendlein and Kelch, 2002).

4.4. Shape-memory cycle tests

The uniaxial shape-memory cyclic tests were conducted up to a nominal strain of 10% and 20%, the results of which are shown in Fig. 5(a) and (b), respectively. The shape fixity ratio (R_f) and shape recovery ratio (R_r) are found to be 95.3% and 84.9%, respectively for an applied strain of 8.7%. Whereas, R_f and R_r for an applied strain of 18% are observed to be 96.2% and 84.4%, respectively. The molecular chains are stretched significantly at higher strains making molecular mobility low and higher chain alignment, which helps in fixing temporary shape or enhances R_f (Xie, 2010; Lendlein and Kelch, 2002). However, large strains damage the polymeric network, leading to poor recovery or decreased R_r (Gall et al., 2002). The biaxial/bulge shape-memory cyclic tests were conducted at applied pressures of 0.45 bar, 0.6 bar, and 0.75 bar (Fig. 6). R_f and R_r for different pressures is discussed in Table 1. As observed in the case of uniaxial shape-memory experiments R_r increases and R_f decreases with increasing pressure/equibiaxial strain. The strain in the bulge test is recorded at the top, which allows uniform deformation of the polymeric chains to exhibit better shape fixity compared to the uniaxial mode. Multiaxial environment enhances shape fixity but at the cost of reduced shape recovery (Liang et al., 2023).

Table 1
R_f and R_r for biaxial shape-memory cyclic tests at different pressures.

Pressure, bar	corresponding equibiaxial strain, %	R_f	R_r
0.45	7.93	96.9	82.1
0.60	11.57	97.1	79.2
0.75	16.29	97.3	75.4

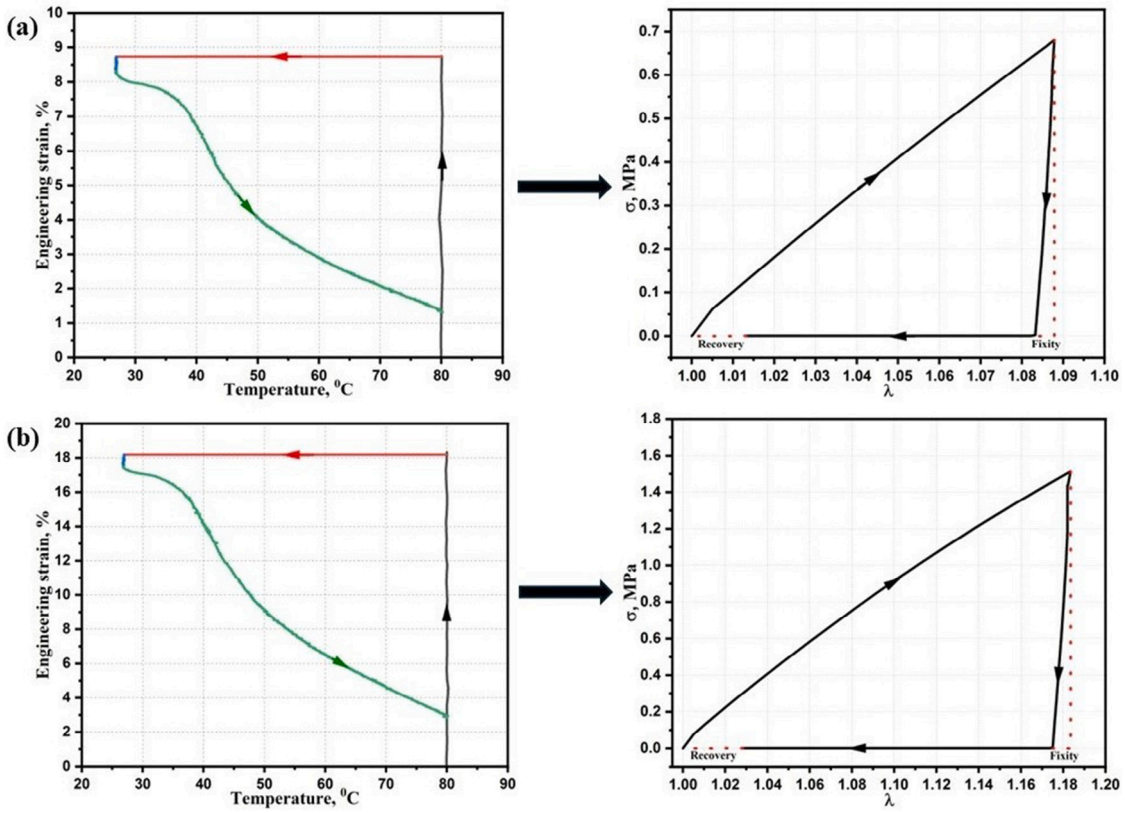

Fig. 5. Strain versus temperature and uniaxial stress versus stretch curves for shape-memory cycle up to strain of (a) 8.7% and (b) 18%. The dotted red lines represent completely ideal case where shape fixity and recovery are 100%.

4.5. Model calibration

Model calibration performed for the bulge test is not enough and we would like to combine it with the results of uniaxial tension tests. For this purpose, we consider stresses at the apex of the membrane obtained in the bulge tests as the experimentally found equibiaxial stresses $\sigma_e^{\exp}$. In addition, we have the experimentally found uniaxial stresses $\sigma_u^{\exp}$. We combine these stresses in the formula for squared residuals $S = \sum_{i=1}^{N}(\sigma_e^{\exp} - \sigma_e)_i^2 + \sum_{i=1}^{N}(\sigma_e^{\exp} - \sigma_e)_i^2$ and minimize it using MATLAB (MathWorks, 2022). Here, σ_u and σ_e are uniaxial and equibiaxial stresses calculated using formulas for uniaxial (Section 3.2.1) and equibiaxial (Section 3.2.2) tension, respectively.

The fitting is performed for glassy and rubbery phases separately. The calibrated parameters are shown in Table 2 and comparative results in Fig. 7. The same material constants are used for shape-memory cyclic experiments. In this sophisticated way we trace failure and shape-memory behavior of SMPs using a single model. The comparative results for uniaxial and equibiaxial tests are shown in Figs. 8 and 9, respectively.

The elastic modulus (E) and cross-link density (ν) for rubbery phase is calculated using the following definitions, where R and T are Gas constant and temperature, respectively (Treloar, 1975; Ogden, 1972)

$$E = \frac{3}{2}\sum_{i=1}^{3}\mu_i\alpha_i, \qquad \nu = \frac{E}{3RT}. \tag{37}$$

The cross-link density for rubbery phase is calculated as 784 $\mathrm{mol/m^3}$ which is lower than that for glassy phase. This observation can be attributed to the fact that in the rubbery phase molecular structure is disordered and polymeric chains are loosely packed, leading to reduced elastic modulus (Mahieux and Reifsnider, 2001). The sacrifice of cross-link density in rubbery phase is to suffice straightening of chain entanglement, which assists shape-memory behavior of the polymer (Jones and Ashby, 2012). The mobility of chains also changes as per phase; Further in rubbery regime the contribution is entropic, while in the glassy regime it is enthalpic. The energy limiter for glassy phase (Φ_g) is 36% higher than rubbery phase (Φ_r), which can be associated with higher cross-link density, stiffness, and strong molecular bonds in glassy phase.

The latter observations regarding molecular-level differences physical perhaps, not structural in different phases motivated us to analyze the effect of void growth (cavitation) on deformation. We use expression for thermoelastic hydrostatic tension (g) during expansion of cavity elaborated in Lev et al. (2019) and write it for SMPs as

$$g = \int_1^{\lambda_{r_i}} \frac{\partial(\mathcal{K}w)/\partial\lambda}{\lambda^3 J^{-1} - 1}\, d\lambda, \tag{38}$$

where $\lambda_{r_i} = r_i/R_i$, and $\lambda = r/R$ — see Fig. 10(a); w, $\mathcal{K}$ and J can be calculated using Eqs. (1), (13), and (18), respectively.

Generally, when we increase the temperature, the stiffness of rubberlike materials increases, which in turn increases critical hydrostatic tension (g_c) corresponding to unstable void growth. It is interesting to see that when we switch from rubbery phase to glassy phase, g_c increases by 183% – Fig. 10(b). The latter observation can be associated with increased stiffness, strong covalent bonds, and compact polymeric chains in glassy phase which favor increment in g_c. However, relaxed polymeric chains and low cross-link density in rubbery phase favor increment in critical stretch, when compared with glassy phase.

5. Conclusions

In the present work we studied the mechanical failure of SMPs both experimentally and theoretically in various tests (from uniaxial and biaxial stress–strain to bulge tests). By failure we meant the onset of

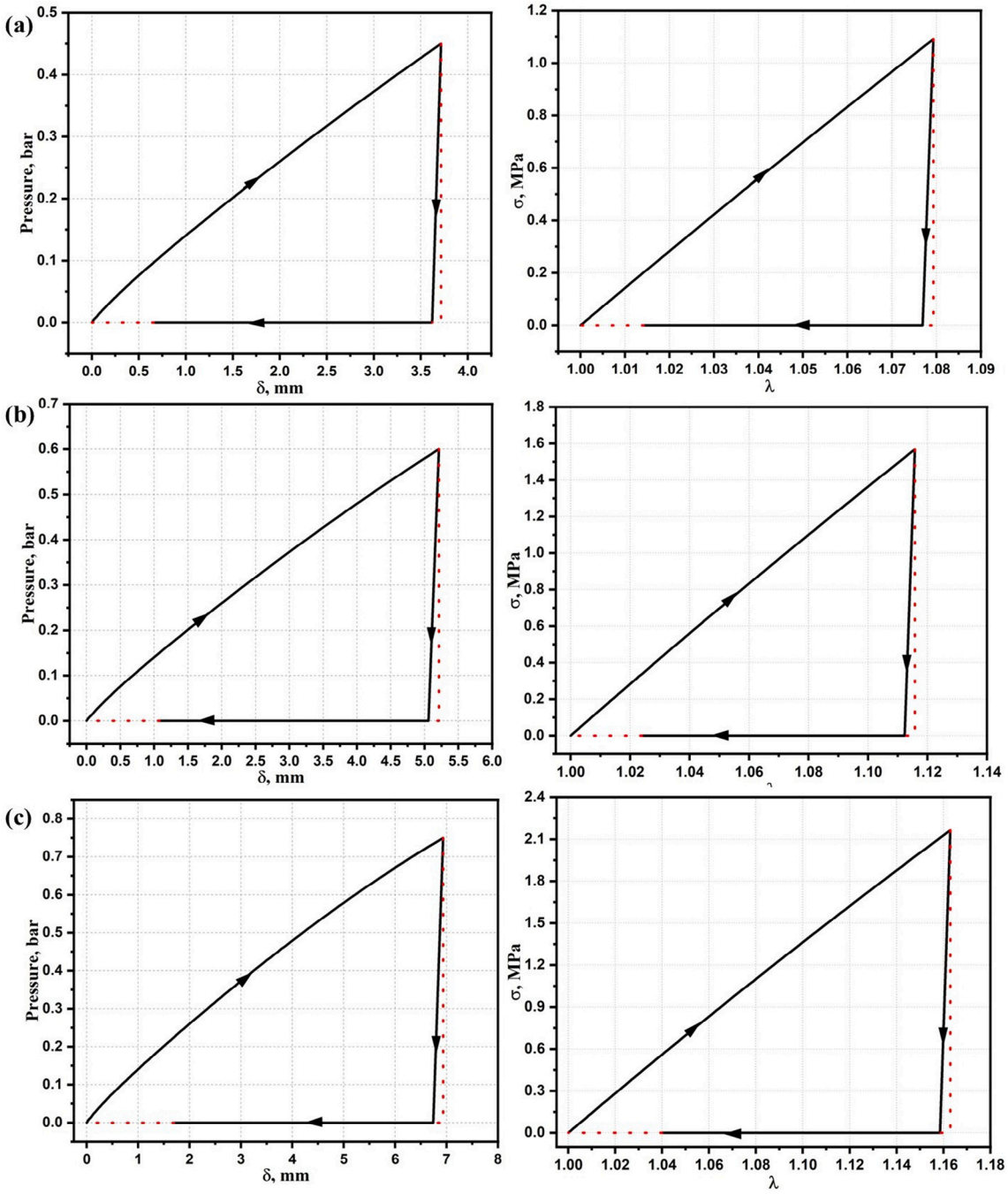

Fig. 6. Pressure versus bulge height and equibiaxial stress versus stretch curves for shape-memory cycle up to pressure of (a) 0.45 bar, (b) 0.6 bar, and 0.75 bar. The dotted red lines represent completely ideal case where shape fixity and recovery are 100%.

damage, limiting the ability of material to bear loads. Traditionally, engineers use the term strength to describe the failure properties of materials. The strength is defined as the maximum achievable stress in uniaxial loading tests. Although the simplicity of such definition is appealing, its use is restrictive and, even, dangerous. Indeed, the maximum tensile stress achievable in uniaxial tension tests of soft materials is usually greater than the maximum tensile stress achievable in equibiaxial tension tests (Volokh, 2025). Thus, design of structural elements made of soft materials based on the traditional concept of strength might be fallacious.

In order to consider material failure properties more accurately, we combined uniaxial and biaxial tension tests. Unfortunately, the classical biaxial tension test is not good for studying failure because the stress–strain state is homogeneous and very sensitive to the boundary conditions – the failure usually starts at the boundary, which is unacceptable. To overcome this obstacle, we used bulge tests, in which thin material specimens are inflated until failure (rupture). Such failure always starts at the apex – in the middle – of the inflating circular membrane and it is not affected by the boundary conditions. The payment for the use of the bulge test is high – it is necessary to solve the inverse boundary value problem iteratively in order to interpret the experimental results correctly. Regretfully, no analytical solutions or procedures are available and sophisticated numerical tools are necessary. We developed and used them.

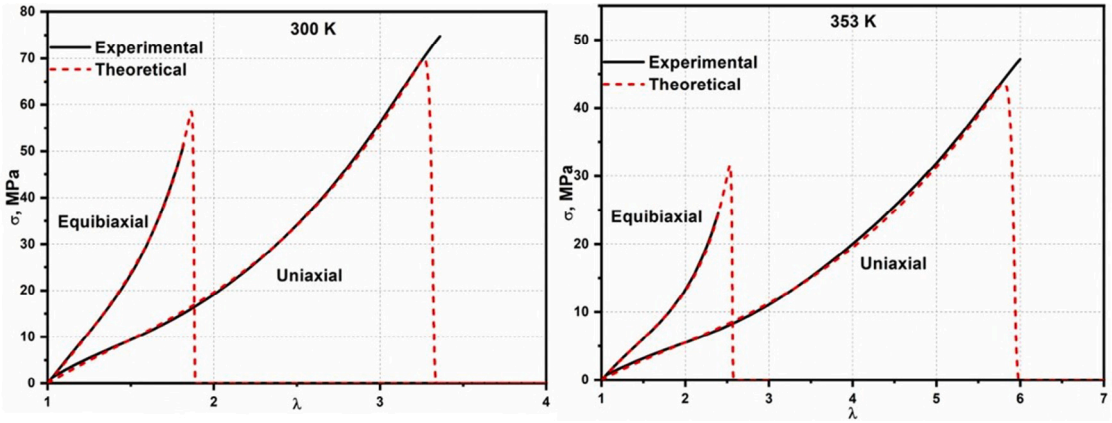

Fig. 7. Comparison between experimental and theoretical results for glassy (left) and rubbery phases (right).

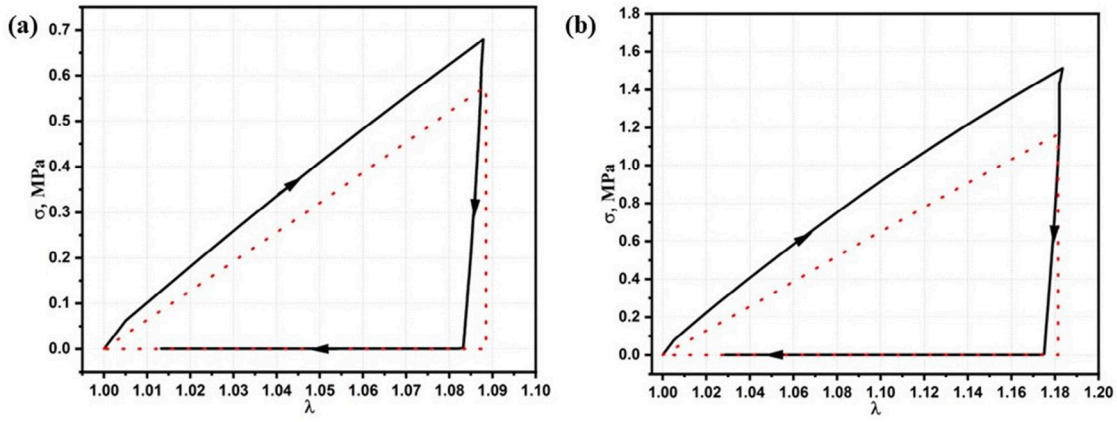

Fig. 8. Comparison between experimental and theoretical results for uniaxial shape-memory tests conducted at strains of (a) 8.7% and (b) 18%.

Table 2
Constitutive model parameters.

Parameter	Value	SI unit
μ_{r1}	−9.99	MPa
μ_{r2}	-2.2×10^{-3}	MPa
μ_{r3}	0.18	MPa
α_{r1}	−0.35	–
α_{r2}	−4.72	–
α_{r3}	2.90	–
Φ_r	19	MPa
m	100	–
μ_{g1}	−9.99	MPa
μ_{g2}	-6.81×10^{-4}	MPa
μ_{g3}	0.73	MPa
α_{g1}	−1.19	–
α_{g2}	−7.88	–
α_{g3}	3.61	–
Φ_g	26	MPa
p	100	–
γ_r	1.34×10^{-4}	K^{-1}
γ_g	7.47×10^{-5}	K^{-1}
c_0	0.019	MPa/K

Our theoretical description of material failure is enforced in the constitutive law via parameters called energy limiters. The limiters indicate the maximum saturation energy that can be stored and dissipated by material from the macroscopic point of view. Microscopically, the limiters represent the average molecular bond energy. The motivation for limiting the stored energy is obvious – the bond energy is bounded and the number of bonds is finite. We note that the bounded stored energy automatically implies the bounded stresses. The latter, in its turn, means that there is no need to impose "strength" as a separate failure criterion – it comes naturally out of the constitutive law.

The described experimental and theoretical approaches were applied to SMPs based on the glass transition specifically. These materials have two phase states: rubber and glassy depending on the temperature under consideration. The deformation and failure properties depend on both the phase and the temperature. We were able to study the temperature effect by performing uniaxial tension and bulge tests (after some preconditioning) inside thermal chamber by varying temperatures. The experimental results were further used for the calibration of the bi-phasic continuum mechanics model. We used hyperelastic models enhanced with the energy limiters depending on the temperature. Remarkably, both glass and rubbery phases could be united in analytical description with a simple switch function. For the sake of theoretical consistency, we also showed how to generalize the model for simulating crack propagation, that is fracture via the damage localization after its onset. We did not do such simulations — they are not usually necessary for design of structures.

In summary, we developed and presented a new experimental–theoretical approach to study and calibrate thermomechanical properties, including both deformation and failure, of shape-memory polymers.

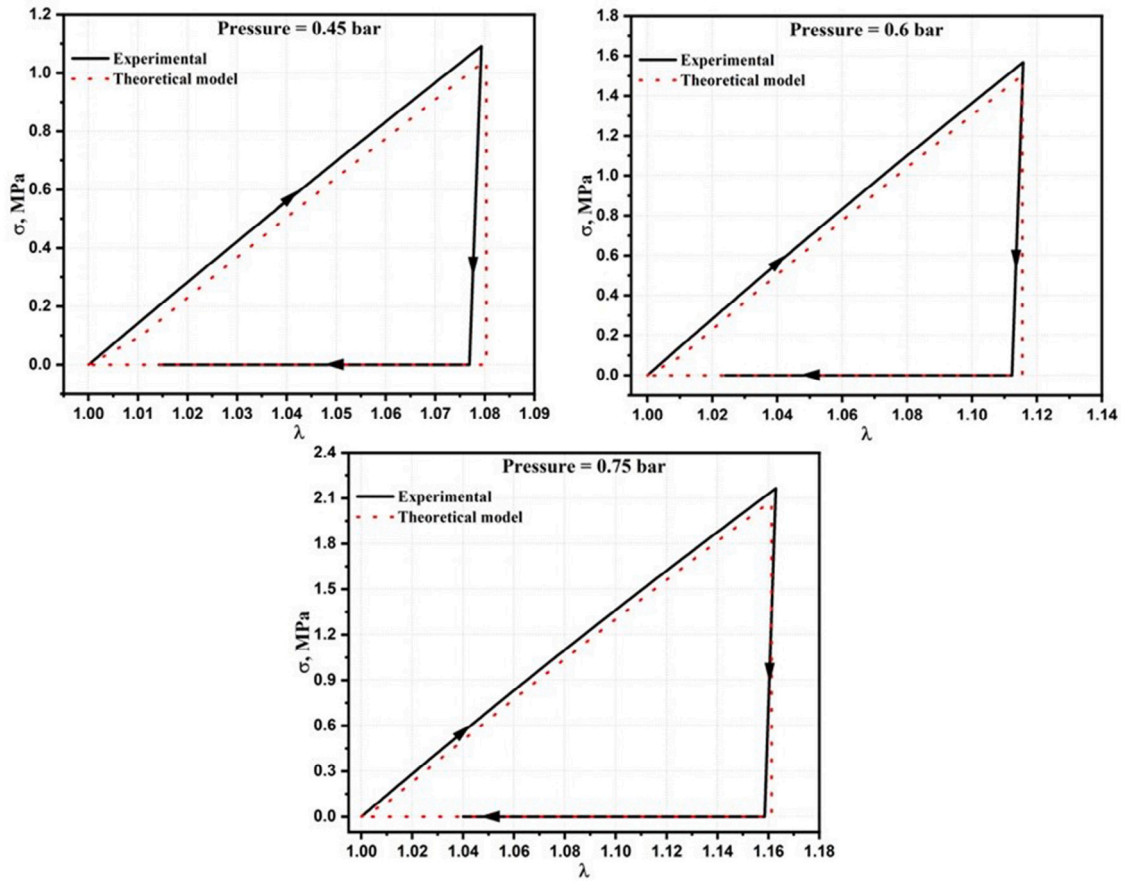

Fig. 9. Comparison between experimental and theoretical results for equibiaxial shape-memory tests conducted at different pressures.

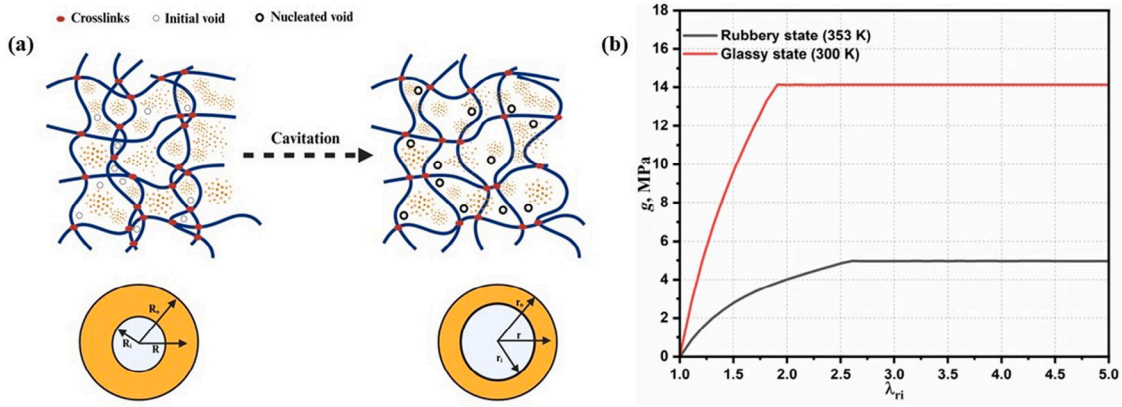

Fig. 10. (a) Void growth in SMPs and (b) Hydrostatic tension versus normalized radius for rubbery and glassy phases.

CRediT authorship contribution statement

Mohit Goswami: Writing – original draft, Validation, Software, Methodology, Investigation, Data curation, Conceptualization. **Matteo Arricca:** Writing – original draft, Software, Methodology, Formal analysis. **Lorenzo Bonetti:** Writing – review & editing, Investigation, Data curation. **Stefano Pandini:** Writing – review & editing, Visualization, Supervision, Investigation. **Giulia Scalet:** Writing – review & editing, Visualization, Supervision, Project administration, Funding acquisition, Conceptualization. **Konstantin Volokh:** Writing – review & editing, Writing – original draft, Supervision, Resources, Project administration, Methodology, Funding acquisition, Conceptualization.

Declaration of competing interest

The authors declare that they have no known competing financial interests or personal relationships that could have appeared to influence the work reported in this paper.

Acknowledgments

The support from the Israeli Ministry of Science and Technology (MOST-0005173) is gratefully acknowledged. This publication was supported by the contribution of the Italian Ministry of Foreign Affairs and International Cooperation under the project "Failure and fracture of shape-memory polymers" (F^2SMP). The authors thank Prof. Eliana

Quartarone and Dr. Daniele Callegari from the Departments of Chemistry, University of Pavia, for access and support with the hot-press.

Data availability

Data will be made available on request.

References

Balakhovsky, K., Volokh, K.Y., 2012. Inflation and rupture of rubber membrane. Int. J. Fract. 177, 179–190.

Boatti, E., Scalet, G., Auricchio, F., 2016. A three-dimensional finite-strain phenomenological model for shape-memory polymers: Formulation, numerical simulations, and comparison with experimental data. Int. J. Plast. 83 (153–177).

Bonetti, L., Natali, D., Pandini, S., Messori, M., Toselli, M., Scalet, G., 2024. 4D printing of semi-crystalline crosslinked polymer networks with two-way shape-memory effect. Mater. Des. 238, 112725.

Foyouzat, A., Bayesteh, H., Mohammadi, S., 2020. A brittle to ductile phase transition fracture analysis of shape memory polymers. Eng. Fract. Mech. 224, 106751.

Foyouzat, A., Bayesteh, H., Mohammadi, S., 2021. Phase evolution based thermomechanical crack closure mechanism of shape memory polymers. Mech. Mater. 160, 103998.

Gall, K., Dunn, M.L., Liu, Y., Finch, D., Lake, M., Munshi, N.A., 2002. Shape memory polymer nanocomposites. Acta Mater. 50 (20), 5115–5126.

Goswami, M., Gupta, P., Lev, Y., Chattopadhyay, S., Volokh, K., 2024. Multiaxial failure of dual-phase elastomeric composites. Eng. Fract. Mech. 312, 110625.

Hu, J., Zhu, Y., Huang, H., Lu, J., 2012. Recent advances in shape–memory polymers: Structure, mechanism, functionality, modeling and applications. Prog. Polym. Sci. 37 (12), 1720–1763.

Jiang, Y., Leng, Q.Y., Yan, Y., Ng, E.L.L., Chee, H.L., Wang, F., Chan, S.Y., Loh, X.J., Wang, J., Chan, B.Q.Y., 2022. 4D printing of Single-Network shape memory polyurethanes with Two-Way actuation properties. ACS Appl. Polym. Mater. 4 (11), 8574–8583.

Jones, D.R., Ashby, M.F., 2012. Engineering materials 2: an introduction to microstructures and processing. Butterworth-Heinemann.

Konale, A., Srivastava, V., 2025. On modeling fracture of soft polymers. Mech. Mater. 206, 105346.

Lendlein, A., Kelch, S., 2002. Shape-memory polymers. Angew. Chem. Int. Ed. 41 (12), 2034–2057.

Lev, Y., Faye, A., Volokh, K., 2019. Thermoelastic deformation and failure of rubberlike materials. J. Mech. Phys. Solids 122, 538–554.

Liang, Z., Li, J., Chen, K., Dong, Y., Yu, C., Kan, Q., 2023. Multiaxial shape memory effect of thermo-induced shape memory polyurethane under proportional tension-torsion loading. Smart Mater. Struct. 32 (7), 075018.

Liu, Y., Gall, K., Dunn, M.L., Greenberg, A.R., Diani, J., 2006. Thermomechanics of shape memory polymers: uniaxial experiments and constitutive modeling. Int. J. Plast. 22 (2), 279–313.

Mahieux, C.A., Reifsnider, K.L., 2001. Property modeling across transition temperatures in polymers: a robust stiffness–temperature model. Polym. 42 (7), 3281–3291.

MathWorks, I., 2022. MATLAB version: 9.13. 0 (R2022b).

Meng, Q., Hu, J., 2009. A review of shape memory polymer composites and blends. Compos. A 40, 1661–1672.

Nguyen, T.D., 2013. Modeling shape-memory behavior of polymers. Polym. Rev. 53 (1), 130–152.

Ogden, R.W., 1972. Large deformation isotropic elasticity–on the correlation of theory and experiment for incompressible rubberlike solids. Proc. R. Soc. A 326 (1567), 565–584.

Ogden, R.W., 1997. Non-linear Elastic Deformations. Courier Corporation.

Qi, H.J., Nguyen, T.D., Castro, F., Yakacki, C.M., Shandas, R., 2008. Finite deformation thermo-mechanical behavior of thermally induced shape memory polymers. J. Mech. Phys. Solids 56 (5), 1730–1751.

Scalet, G., 2020. Two-way and multiple-way shape memory polymers for soft robotics: An overview. Actuators 9 (1), 10.

Tobushi, H., Hara, H., Yamada, E., Hayashi, S., 1996. Thermomechanical properties in a thin film of shape memory polymer of polyurethane series. Smart Mater. Struct. 5 (4), 483.

Tobushi, H., Hashimoto, T., Hayashi, S., Yamada, E., 1997. Thermomechanical constitutive modeling in shape memory polymer of polyurethane series. J. Intell. Mater. Syst. Struct. 8 (8), 711–718.

Tobushi, H., Hashimoto, T., Ito, N., Hayashi, S., Yamada, E., 1998. Shape fixity and shape recovery in a film of shape memory polymer of polyurethane series. J. Intell. Mater. Syst. Struct. 9 (2), 127–136.

Treloar, L.G., 1975. The Physics of Rubber Elasticity. OUP Oxford.

Volk, B.L., Lagoudas, D.C., Chen, Y.-C., 2010. Analysis of the finite deformation response of shape memory polymers: II. 1D calibration and numerical implementation of a finite deformation, thermoelastic model. Smart Mater. Struct. 19 (7), 075006.

Volokh, K., 2011. Characteristic length of damage localization in rubber. Int. J. Fract. 168, 113–116.

Volokh, K.Y., 2025. Modeling Failure and Fracture of Soft Solids and Fluids. Springer.

Xia, Y., He, Y., Zhang, F., Liu, Y., Leng, J., 2021. A review of shape memory polymers and composites: Mechanisms, materials, and applications. Adv. Mater. 33 (6), 2000713.

Xie, T., 2010. Tunable polymer multi-shape memory effect. Nat. 464 (7286), 267–270.

Yan, C., Li, G., 2022. Tutorial: Thermomechanical constitutive modeling of shape memory polymers. J. Appl. Phys. 131 (11).

Zhao, W., Liu, L., Lan, X., Leng, J., Liu, Y., 2023. Thermomechanical constitutive models of shape memory polymers and their composites. Appl. Mech. Rev. 75 (2), 020802.